Quasi-Periodic Occultation by a Precessing Accretion Disk and Other Variabilities of SMC X-1

Patrick Wojdowski[1], George W. Clark[1], and Alan M. Levine
Center for Space Research,Massachusetts Institute of Technology, Cambridge, MA 02139
Jonathan W. Woo
Harvard-Smithsonian Center for Astrophysics, Cambridge, MA 02138
Shuang Nan Zhang
Universities Space Research Association/Marshall Space Flight Center, ES 84, Huntsville, AL 35812

Received _____; accepted _____

arXiv:astro-ph/9801168v1 16 Jan 1998

[1]Department of Physics, Massachusetts Institute of Technology, Cambridge, MA 02139

ABSTRACT

We have investigated the variability of the binary X-ray pulsar, SMC X-1, in data from several X-ray observatories. We confirm the $\sim$ 60-day cyclic variation of the X-ray flux in the long-term monitoring data from the *RXTE* and *CGRO* observatories. X-ray light curves and spectra from the *ROSAT*, *Ginga*, and *ASCA* observatories show that the uneclipsed flux varies by as much as a factor of twenty between a high-flux state when 0.71 second pulses are present and a low-flux state when pulses are absent. In contrast, during eclipses when the X-rays consist of radiation scattered from circumsource matter, the fluxes and spectra in the high and low states are approximately the same. These observations prove that the low state of SMC X-1 is not caused by a reduction in the intrinsic luminosity of the source, or a spectral redistribution thereof, but rather by a quasi-periodic blockage of the line of sight, most likely by a precessing tilted accretion disk. In each of two observations in the midst of low states a brief increase in the X-ray flux and reappearance of 0.71 second pulses occurred near orbital phase 0.2. A similar brief flux increase near orbital phase 0.2 was observed during a low-state observation that did not have sufficient time resolution to detect 0.71 second pulses. These brief increases result from an opening of the line of sight to the pulsar that may be caused by wobble in the precessing accretion disk. The records of spin up of the neutron star and decay of the binary orbit are extended during 1991-1996 by pulse-timing analysis of *ROSAT*, *ASCA*, and *RXTE* PCA data. The pulse profiles in various energy ranges from 0.1 to $>$ 21 keV are well represented as a combination of a pencil beam and a fan beam. Finally, there is a marked difference between the power spectra of random fluctuations in the high-state data from the *RXTE* PCA below and above 3.4 keV. In the higher energy range the spectrum has a sharp break at 3.3 Hz, with fitted power law indices of 0.45 and 1.76 below and above the break. No break is evident in the power spectrum below 3.4 keV, and the fitted power law index is 0.51. In both spectra there is a positive deviation from the fitted power law around 0.06 Hz that may be QPO.

1. INTRODUCTION

SMC X-1, located in the Small Magellanic Cloud (SMC), is the most luminous and rapidly spinning of the persistent accretion-powered X-ray pulsars. Its X-ray flux pulses with a 0.71 second period, it is eclipsed by its B0 supergiant companion for $\sim$ 15 hours of the 3.892-day orbit, and its uneclipsed X-ray flux exhibits aperiodic variations on time scales from tens of milliseconds to months. Its rotation rate is increasing on a time scale of 10^3 yr, and its orbit is decaying on a time scale of 10^6 yr. With a well-determined distance, small amount of intervening matter, and extreme values of luminosity and spin rate, SMC X-1 is a well-placed and particularly interesting object for detailed studies.

X-rays from "an extended region or set of sources" in the SMC were discovered in a rocket observation by Price et al. (1971). Leong et al. (1971) identified a discrete source in the "wing" of the SMC in *Uhuru* observations and named it SMC X-1. Further analysis of these and additional *Uhuru* observations by Schreier et al. (1972) revealed the eclipse phenomena which established its binary nature. The identification of its optical counterpart as the B0I star Sk 160, suggested by Webster et al. (1972), was confirmed by Liller (1973) who observed an optical intensity variation with the same period as that of the X-ray eclipses. Lucke (1976) discovered the X-ray pulsations in rocket and Apollo satellite observations. Accurate values of the orbital elements of SMC X-1 and rates of spin-up due to accretion

torque were derived by pulse-timing analysis of *SAS 3* data by Primini, Rappaport, & Joss (1977) and of *Ariel V* data by Davison (1977). Measurements of the velocity curve of Sk 160 by optical spectroscopy (Hutchings et al. 1977; Reynolds et al. 1993), combined with the velocity curve of the pulsar, yielded narrow limits on the masses of both components of the binary system. An X-ray burst lasting ~ 80 s and aperiodic variability on time scales ranging from tens of milliseconds to hours were reported from *EXOSAT* observations by Angelini, Stella, & White (1991). Levine et al. (1993) (hereinafter LRD) determined the rate of orbital decay in a comprehensive analysis of the eclipse center times derived by pulse-timing analysis of data from various satellite observations through 1989, including their own observations with the *Ginga* satellite. Their publication includes a discussion of the implications of the observed decay for the orbital dynamics of the system.

The circumstellar environment of the Sk 160/SMC X-1 system has been the subject of several investigations. Van Paradijs & Zuiderwijk (1977) attributed anomalies in five-color photometry of Sk 160 to the optical emission from an accretion disk around the neutron star, and Tjemkes, Zuiderwijk, & van Paradijs (1986) interpreted the optical light curve in terms of ellipsoidal variations, disk emission, and X-ray heating effects. Hammerschlag-Hensberge, Kallman, & Howarth (1984) found evidence in UV spectra obtained from *IUE* of the influence of X-ray illumination on the stellar wind of Sk 160 in the form of a deviation from spherical symmetry of the outflow and an anomalously low terminal velocity compared to stars of similar spectral type. Blondin & Woo (1995) modeled the wind dynamics of the Sk 160/SMC X-1 system in three-dimensional hydrodynamical calculations which took account of the effects of X-ray ionization. Model light curves and spectra derived by Monte Carlo calculation of X-ray propagation through the stellar wind conformed well to the light curves and spectra of SMC X-1 derived from *Ginga* and *ROSAT* observations, and in particular with the data obtained during eclipse transitions when the X-ray line of sight passes close to the surface of Sk 160 (Woo et al. 1995).

Extended periods of very low X-ray flux of the uneclipsed source have been reported in observations with *Uhuru* (Schreier et al. 1972), *Copernicus* (Tuohy & Rapley 1975), *Ariel V* (Cooke 1978), and *COS-B* (Bonnet-Bidaud & van der Klis 1981). An extended period of exceptionally high flux, beginning in 1970 September and lasting ~ 100 days, was reported from a three-year record of observations by the *Vela 5B* monitor (Whitlock & Lochner 1994). Gruber & Rothschild (1984), in particular, reported a large amplitude high-low state variation in the X-ray flux in data from three ~ 80 day observations with the UCSD/MIT instrument on *HEAO 1* in 1977 and 1978. They noted that the observed variations could be ascribed to either a quasi-periodic cycle with a duration of about sixty days or to a band-limited red noise process of unspecified origin; a strictly periodic variation was not consistent with their observations. They also suggested two possible physical mechanisms for a cyclic variation — intrinsic luminosity variation due to unstable mass transfer or periodic occultation by a precessing tilted accretion disk.

In this paper we address several topics concerning the variability of SMC X-1 and the evolution of the Sk 160/SMC X-1 system. The observations and data reduction are described in §2. In §3, we present long-term monitoring data from the All-Sky Monitor (ASM) on the *Rossi X-ray Timing Explorer* (*RXTE*) and the Burst and Transient Source Experiment (BATSE) on the *Compton Gamma-ray Observatory* (*CGRO*) that confirm the ~ 60-day cyclic variability of the X-ray flux (brief reports of this result were made by Zhang et al. (1996) and Levine et al. (1996)). We then present an analysis of the X-ray light curves and spectra derived from various pointed-mode observations by the *ASCA*, *ROSAT*, *Ginga*, and *RXTE* observatories for the purpose of determining the cause of the cyclic variability. In §4, the records of spin-up of the neutron star and decay of the binary orbit are extended from mid 1991

to early 1996 with results derived by pulse-timing analysis of data from *ROSAT*, *ASCA* and *RXTE*. Pulse profiles in several energy ranges from 0.1 to > 21 keV are derived from these data, and modeled by a pulsar radiation pattern consisting of a pencil beam and a fan beam. Finally, in §5 we compare the power density spectra of the random fluctuations of the high-state flux in the high and low-energy portions of the data recorded by *RXTE*.

2. OBSERVATIONS AND INITIAL DATA REDUCTION

Bright X-ray sources have been monitored with the BATSE instrument in the 20-100 keV range since April of 1991 and with the ASM instrument in the 1.5-12 keV range since 20 February 1996. The BATSE instrument has been described by Fishman et al. (1994), and the ASM instrument by Levine et al. (1996). Source intensities are derived from BATSE data by fitting the predicted changes in count rates caused by earth occultations to the measured rates (Harmon et al. 1992). Intensities of known sources are derived from ASM data by fitting predicted shadow patterns cast by coded masks to observed patterns recorded by position-sensitive proportional counters.

The *Ginga* data were obtained with the Large Area Counter (LAC) comprised of 8 proportional gas counters with a peak total effective area of 4000 cm^2, a mechanically-collimated field of view of $1.1^\circ \times 2.0^\circ$ FWHM, an energy range from 1.5 to 36 keV, and an energy resolution of 20% FWHM at 5.9 keV. The *Ginga* observatory has been described by Makino (1987) and details of the LAC by Turner et al. (1989).

Data from four *ROSAT* imaging observations were obtained with the Position Sensitive Proportional Counter (PSPC) in the focal plane of the X-ray telescope (XRT). The *ROSAT* mission has been described by Trümper (1983) and the XRT-PSPC system by Pfeffermann et al. (1987) and Aschenbach (1988). The XRT-PSPC had an angular resolution of $\sim 25''$, and was sensitive in the energy range from 0.1 to 2.5 keV. We denote the four *ROSAT* observations with the labels "1", "2", "3", and "C". In the numbered observations, SMC X-1 was close to the center of the imaged field of view. Observation "C" was part of a survey of the SMC (Kahabka & Pietsch 1996); in that observation SMC X-1 was $\sim 40'$ off axis.

The *ASCA* imaging data were obtained with the Solid-state Imaging Spectrometer (SIS) and the Gas Imaging Spectrometer (GIS) which are sensitive in the energy range from approximately 0.3 to 12 keV. The *ASCA* observatory has been described by Tanaka, Inoue, & Holt (1994).

The pointed-mode *RXTE* data were obtained during the in-orbit checkout (IOC) period of operation with the Proportional Counter Array (PCA) which has a peak effective area of 7000 cm^2, a mechanically-collimated 1° FWHM field of view, 18% energy resolution at 6 keV, and an energy range from 2 to 60 keV (Jahoda et al. 1996).

Table 1 summarizes the times and exposures of the pointed observations and the "state" of SMC X-1 in the high-low cycle as defined below.

2.1. Background Subtraction of Pointed Observations

Background rates in the source region of the images produced by the *ROSAT* and *ASCA* observatories were estimated from the count rates in separate nearby regions. For *ROSAT* observations 1, 2, and 3 we chose the source region to be a circle of radius $150''$ and the background region to be an annulus of inner radius $150''$ and outer radius $300''$. For the poorly focused *ROSAT* C observation, we chose

the source region to be a circle of radius 262.5″ and the background region to be an annulus with radii of 262.5″ and 487.5″. We excluded from both the background and source regions a circular region of radius 150″(188″ for the off-axis pointing) centered on the foreground coronal star HD 8191 - a weak soft X-ray source. Also, we excluded a circular region of radius 150″ around the transient source RX J0117.6-7330 (Clark et al. 1997) in the two observations (2 & 3) in which it appeared.

In the GIS image of the *ASCA* observations, we chose the source region to be a circle of radius 383″ and the background region to be an annulus of radii 383″ and 766″. In observation 2, a circular region of radius 150″ around HD 8191was removed from both the source and background regions. In the SIS image, we chose the source region to be a square 380″ on a side centered on SMC X-1 and used the remainder of the chip as the background region. HD 8191 was not in the field of view of the SIS in these observations.

Background corrections to the *Ginga* data were made according to the algorithm of Hayashida et al. (1989). Background corrections to the *RXTE* data were derived from the earth-occulted count rates which are listed in Table 2 together with the on-target rates in seven energy ranges. We note that the *ROSAT* images show several faint and soft sources near SMC X-1 that were within the *Ginga* and *RXTE* fields of view. No corrections to the background rates were made for these sources because their total contribution to the *Ginga* count rate was less than a few percent of the SMC X-1 eclipsed count rate (Woo et al. 1995), and less than one percent of the *RXTE* rates.

3. QUASI-PERIODIC HIGH-LOW FLUX VARIATION

3.1. Long-Term Monitoring Observations

Figure 1 displays the X-ray light curves of SMC X-1 measured by the ASM and BATSE instruments during times when the pulsar was uneclipsed and in the orbital phase range between 0.1 and 0.9 relative to eclipse center. The ASM data are binned in intervals of the 3.89-day orbital period, and the BATSE data in five-day intervals.

A cyclic flux variation on a time scale of $\sim$ 60 days is clearly evident in the ASM light curve. To quantify the duration of each cycle, which appears to be variable, we defined times of the beginning and end of each high state to be when the count rate increased/decreased to 2 counts s^{-1}. We determined these times by interpolating between successive points with values below and above, or above and below, 2 counts s^{-1}. The times between successive rises and falls defined in this way are plotted against cycle number in Figure 2 where they are seen to range from below 50 to above 60 days with a generally decreasing trend. The ASM light curve shows that the flux often increased relatively quickly at the beginning of each high state and decreased more slowly at the end.

To test for the presence of cyclic variability in the BATSE data, we divided the data into four subsets of equal duration and folded each subset into 5 phase bins with trial periods between 30 and 100 days. In this process, the mean flux and its standard deviation in each phase bin were calculated using the inverses of the variances of the individual measurements as weights. At each trial period, we calculated the reduced χ^2 statistic of the light curve assuming that no signal was present. The values of the reduced χ^2 statistic are plotted in Figure 3 for each quarter of the BATSE light curve and for the entire BATSE light curve. Also shown are the results of the same analysis applied to the entire ASM light curve. Leahy et al. (1983) showed that if a sinusoidal signal with a fixed period, P, is present in the light curve, such a folding analysis will show a peak centered at that period with a FWHM of P^2/T, where T is the length of the observation. In Figure 3 the horizontal bars show the expected FWHM

of a sinusoidal signal with a 55-day period. We note that the positions of the peaks shift and some of peaks are substantially wider than the horizontal bars. These features, together with the drift of the time since last increase/decrease in the ASM light curve (Figure 2), are strong evidence for the absence of a long-term coherent periodicity in these data sets. Instead, the observed cyclic variation can be best characterized as quasi-periodic with recurrence times that wander between ∼50 and ∼60 days. Attempts to examine the variation of the cycle more closely in the BATSE light curve by smoothing and by correlation with a sine wave were inconclusive, presumably due to the low signal-to-noise ratio in the data.

3.2. Short-Term Pointed Observations

Background-subtracted count rates, derived from the *Ginga*, *ROSAT*, *ASCA*, and *RXTE* PCA observations, are plotted in Figure 4 against orbital phase. We multiplied the background-subtracted count rates of the off-axis *ROSAT* observation by a factor of 1.7 to compensate for the reduction in effective area relative to the on-axis observation. So that the *Ginga* and *ASCA* count rates may be directly compared, we show the count rates from the pulse height channels which correspond to the energy range 1-10 keV. For the *ASCA* GIS, these are PI channels 85 through 850. For the *Ginga* LAC these are channels 3 through 18 in the MPC-2 mode data and 1 to 4 in the MPC-3 mode data.

With the exception of the *Ginga* observation, which occurred before the beginning of the BATSE light curve, all of the pointed observations discussed in this paper occurred during the time of the BATSE observations, and before the *RXTE* ASM observations. Unfortunately, the signal-to-noise ratio of the BATSE light curve is not large enough to allow certain determination of the phases in the flux cycle at which the individual pointed observations occurred. Furthermore, because of the quasi-periodic nature of the cycle, it is not possible to extrapolate backwards from the ASM light curve. However, the ASM light curve shows that the X-ray flux averaged over the uneclipsed portion of each binary orbit rises and falls smoothly over each cycle. Therefore, we are confident that the observed out-of-eclipse flux of the source, as it is revealed in the light curves, is a reliable indicator of the state of the source.

The contrast between the high and low states of SMC X-1 is most clearly demonstrated by the various *ROSAT* observations. Where observation 1 and the region C observation overlap in orbital phase outside of eclipse, they differ in (corrected) count rate by a factor of at least 20. We therefore identify *ROSAT* observation 1 as having occurred during the high state and the region C observation as having occurred during the low state. The light curve of *ROSAT* observation 2 behaves like that of the region C observation where the two overlap so we identify this observation as having occurred during the low state as well. Outside of eclipse, *ROSAT* observation 3 shows a count rate comparable to that of observation 1, so we identify it as having occurred during the high state.

The two *ASCA* observations also differ by a factor of about twenty in their out-of-eclipse count rates, so we assume *ASCA* observation 1 occurred during the high state and *ASCA* observation 2 occurred during the low state. However, the decline in the count rate in observation 1 beginning near orbital phase 0.5 may be a transition to the low state. In the *Ginga* observation, the out-of-eclipse behavior and count rate is comparable to *ROSAT* observation 1 and *ASCA* observation 1, so we conclude it also occurred during the high state. The brief *RXTE* PCA observation near orbit phase 0.5 clearly occurred during a high state.

Interesting features of the low-state light curves derived from the *ROSAT* observations 2 and C are the increases in the count rates near orbital phase 0.25. In both cases, 0.71 second pulsations are present

during the increase. A similar turn-on may be seen in the light curve (not shown herein) derived from the *ROSAT* All-Sky Survey (Kahabka & Pietsch 1996), although those data do not have sufficient time resolution to permit a test for the presence of pulsations. *ROSAT* observation 2 ends near phase 0.3 with this increase. The *ROSAT* C observation has a gap from phase 0.3, where the count rate is increasing, to phase 0.58 (plotted at phase -0.42), where the count rate is lower than before.

In Figure 5 we plot the photon number spectra of SMC X-1 from all the observations during the in-eclipse portions of the binary orbit (orbital phase -0.07 to +0.07). For the purpose of comparing these spectra, we fitted all of them simultaneously with the following model spectrum that consists of the sum of a black-body spectrum and a power law with a high energy cutoff together with interstellar absorption:

$$I(E) = \exp[-\sigma(E)N_{\rm H}][f_{\rm bb}(E) + f_{\rm pl}(E)], \tag{1}$$

where

$$\begin{aligned} f_{\rm bb}(E) &= I_{\rm bb}(E/E_{\rm bb})^2(e-1)[\exp(E/E_{\rm bb})-1]^{-1}, \\ f_{\rm pl}(E) &= I_{\rm pl}(E/1{\rm keV})^{-\alpha} \times \left\{ \begin{array}{ll} 1, & E < E_{\rm c} \\ \exp\left[-\frac{E-E_{\rm c}}{E_{\rm f}}\right], & E \geq E_{\rm c} \end{array} \right\}. \end{aligned}$$

$I_{\rm bb}$ is the the intensity of the blackbody component at $E = E_{\rm bb}$, $I_{\rm pl}$ is the intensity of the power law component at $E = 1$ keV, and $\sigma(E)$ is the photoelectric absorption cross section of cold matter (Morrison & McCammon 1983). The results of the fit are given in Table 3. The convolutions of this model with each of the instrument responses are plotted in Figure 5 along with the corresponding observed spectra. The instrument response for the *ROSAT* C observation includes the reduced efficiency at the off-axis location.

The high-low state identifications we have inferred from the observed fluxes leave no doubt that the spectra displayed in Figure 5 include instances from both the high and low states during the eclipse when the only X-rays detected are those that have been scattered from circumsource matter. Since these five spectra show no more than a factor of two difference in flux at any X-ray energy, we conclude that the average illumination of the circumsource matter varied little between the high and low states. Moreover, all five spectra have similar shapes. Thus, the cause of the cyclic variation cannot be either a variation in the intrinsic luminosity of SMC X-1 or a redistribution of the luminosity across the spectrum. We conclude that the cause of the cyclic variation between states of high and low flux is a quasi-periodic blockage of the line of sight. The same conclusion regarding the cause of the long-term cyclic variation in the X-ray flux of LMC X-4 has been drawn on the basis of similar evidence (Woo, Clark, & Levine 1995).

3.3. Motions of the Accretion Disk

Shortly after discovery of the 35-day high-low state variation in Her X-1, Katz (1973) suggested that if the rim of the neutron star's accretion disc does not lie in the plane of the binary orbit, then the plane of the rim will precess due to the gravitational force of the companion star. Katz argued that if the rim is sufficiently tilted, it will periodically block the line of sight to the neutron star, causing the observed cyclic high-low variation. His expression for the forced precession period, $P_{\rm f}$, of a ring of non-interacting particles can be written in the form

$$P_{\rm f} = \frac{4}{3} P_{\rm b} \left(\frac{R_{\rm L}}{R_{\rm r}}\right)^{3/2} \left[\frac{0.6q^{2/3} + \ln(1+q^{1/3})}{0.49q^{2/3}}\right]^{3/2} (q+q^2)^{1/2} (\cos\beta)^{-1}, \tag{2}$$

where $P_{\rm b}$ is the binary orbital period, $R_{\rm L}$ is the volume-averaged radius of the Roche lobe, $R_{\rm r}$ is the ring radius, q is the ratio of the neutron star mass to the companion star mass, and β is the tilt angle of the ring with respect to the plane of the binary orbit. The quantity in square brackets is an approximate expression for the ratio of the binary separation to the Roche lobe radius (Eggelton 1983).

Analyses of the optical light curves of Sk 160/SMC X-1 indicate that the accretion disk radius is ~ 0.7 to 1.0 times the Roche lobe radius (Howarth 1982; Tjemkes, Zuiderwijk, & van Paradijs 1986; Khruzina & Cherepashchuk 1987). Setting $R_{\rm r}/R_{\rm L} = 0.7$, $q = 0.0909$ (Reynolds et al. 1993), $P_{\rm b} = 3.892$ days, and $\cos\beta \approx 1$, we find the precession period predicted by equation 2 is 31 days or 0.56 times the typical observed cycle time of 55 days. The optical light curves of the two other X-ray binaries with clear quasi-periodic high-low state cycles, Her X-1 and LMC X-4, also indicate that their accretion disks nearly fill the Roche lobes of their neutron stars (Gerend & Boynton 1976; Ilovaisky et al. 1984; Heemskerk & van Paradijs 1989). The corresponding precession periods (assuming $R_{\rm r}/R_{\rm L} = 0.7$ and $\cos\beta \approx 1$) are 0.56 and 0.35 times the observed high-low cycle periods of Her X-1 and LMC X-4, respectively. Thus, in all three cases a simple model of an occulting rim of non-interacting particles predicts precession periods substantially less than the observed high-low cycle times.

Numerous theoretical investigations of the effects of the accretion rate, viscosity, and X-ray illumination on the creation of warp and tilt in the disk and on the precession rate have been carried out. Among these investigations we note in particular the work of Iping & Petterson (1990). They made numerical simulations with results that showed stable precessing disks with quasi-periods that could be adjusted to fit observations by appropriate choices of the accretion rate, the conversion efficiency with which accretion energy is converted into X-rays, and the viscosity parameters. Pringle (1996) confirmed their results with a more rigorous treatment, and showed that a warp instability due to radiation pressure will develop outside a critical radius which is $\approx 3 \times 10^8$ cm for a neutron star. The radius of the Roche lobe in SMC X-1 is $\approx 2.9 \times 10^{11}$cm so the accretion disk is clearly large enough to be unstable to warping. Thus it appears that a detailed model of a precessing tilted accretion disk could provide a quantitative explanation for the observed high-low cycle of SMC X-1.

It is unlikely that random flares were the cause of the short-term flux increases observed near orbital phase 0.25 in the three low-states observations. The presence of 0.71 second pulses in the *ROSAT* 2 and C observations shows that the increased flux came directly from the neutron star. It is also unlikely that the increase in the *ROSAT* C observation was the beginning of a high-state because a decrease followed soon after, and because the observation occurred only ten days after the source was observed to be in a high state in *ROSAT* observation 1. The ASM light curve shows that low states typically last for 15-20 days. Thus the *ROSAT* C observation probably occurred in the early part of a low state. These increases are reminiscent of the low-state turn-ons in Her X-1 which occur near orbital phases 0.2 and 0.7 (cf. Fig. 2 of Priedhorsky & Holt 1987), and which have been attributed (Levine & Jernigan 1982) to a wobble which may be a common feature of precessing accretion disks. Further observations of SMC X-1 are needed to determine the regularity and nature of its low-state turn-ons.

4. PULSE-TIMING ANALYSIS OF SPIN UP AND ORBITAL DECAY

4.1. Observations and Analysis

We carried out pulse timing analysis of the *ROSAT*, *ASCA*, and *RXTE* PCA data to extend previously published results on the spin up of the neutron star and decay of the binary orbit through 1996 January. The *ROSAT* and *ASCA* data consist of the energy, image position, and readout time of each photon

detected in an image of SMC X-1. The time resolution of the *ROSAT* data is a few ms, and the time resolution of the *ASCA* data is 1/16 s. The *RXTE* data consist of the counts accumulated by the PCA in rebinned time intervals of 1/64 s and five energy channels from 2 to > 21 keV.

None of our six pointed observations span a sufficient portion of the SMC X-1 orbit to permit an independent determination of all of the orbital parameters and the rate of change of the pulse frequency. The *ROSAT* 2 and C observations had such brief exposures to the pulsed flux that the data were only sufficient to constrain the pulse frequency when the orbital phase (measured from eclipse center for a circular orbit) was fixed at the value inferred from the other observations. We restricted the timing analysis of the other four observations to determinations of the intrinsic pulse frequency and orbital phase at the start of each observation, while the other orbital parameters were fixed at the values derived by LRD from observations of longer duration. From the orbital phases we derived the center times of the preceding eclipses. These were combined with the previous eclipse center times quoted by LRD in a redetermination of the orbital decay rate.

To obtain initial estimates of the orbital phase, ϕ_0, and intrinsic pulse frequency, f, at the start of an observation, we searched a two-dimensional array of phase and frequency for the pair of values that maximized the fractional amplitude of the folded pulse light curve derived from the entire set of solar system barycentric X-ray arrival times corrected for orbital delay. The delay-corrected arrival time of the ith photon, t'_i, was derived from its observed arrival time, t_i, by iterative solution of the equation

$$t'_i = t_i - a_{\rm x} \sin i \cos(2\pi \frac{t'_i}{a_1} + \phi_0) \tag{3}$$

where the quantities $a_{\rm x} \sin i$ and a_1 were fixed at the values found by LRD and listed in Table 5. The change in these values, implied by the rate of orbital decay measured by LRD, had a negligible effect on the delays computed for the present data.

We refined the estimated values of ϕ_0 and f by the following procedure aimed at obtaining a sequence of accurate pulse arrival time delays to which calculated orbital delays could be fitted by adjustment of the orbital phase. A portion of the delay-adjusted data was folded at the estimated frequency, and a 12-term Fourier series was fitted to the resulting pulse profile to form a template profile. The data were then divided into a number of subsets, and each subset was folded with the estimated frequency to obtain its pulse profile. Each profile was cross-correlated with the template to determine its relative phase shift due to errors in the estimated values of ϕ_0 and f. From the phase shift of the jth profile we computed the difference between the actual corrected arrival time of a pulse near the mean arrival time, T_j, of the data subset and the expected corrected arrival time based on the estimated frequency. We call $\tau(T_j)$ the sum of that difference and the orbital delay at T_j calculated with the estimated ϕ_0. The quantity $\tau(T_j)$ is equal to the sum of the true orbital delay and the time equivalent, $(T_j - T_0)\delta f/f$, of the portion of the phase shift due to the error, δf, of the estimated value of f. A least-squares fit of calculated values of $\tau(T_j)$ to the set of measured values was made by adjustment of ϕ_0 and δf. This procedure was repeated, each time using improved estimates of the orbital phase and frequency to compute a new template and new values of $\tau(T_j)$ until there was no further improvement in the least-squares fit, and no significant trend away from a zero shift in pulse phase between the template and the subset pulse profiles.

In Figure 6 we show plots of the final pulse arrival time delays together with the fitted curves and deviations of the fits. The *ROSAT* 1 and 3 and the *ASCA* 1 observations yielded well-constrained values of the intrinsic pulse period $P = 1/f$ and eclipse center times. In spite of the high statistical

accuracy of the *RXTE* data, the shortness of the observation resulted in relatively large and correlated uncertainties in the eclipse center time and intrinsic pulse frequency.

The quadratic function of orbit number defined by LRD was fitted to the set of eclipse center times which includes the four new ones derived in this work and the seven previous ones listed in their paper and reproduced in Table 4. The result is shown in Figure 7 as a plot of the measured deviations from a linear function of orbit number against time. The fitted values of the coefficients are listed in Table 5 together with the previous values of LRD with which they are entirely consistent.

The pulse periods from this and previous studies are plotted against time in Figure 8 together with the deviations from a fitted quadratic function of time with the coefficients listed in Table 6. We note that every measurement of the pulse period of SMC X-1 has yielded a value lower than the previous measurement. Although the magnitude of the rate of change of the period appears to be decreasing, the absence of any observed episodes of torque reversal indicates that the accretion flow has never slowed enough to allow the inner edge of the accretion disk to retreat to the corotation radius where braking action would be expected to occur.

4.2. Variation of the Pulse Profile with Time and Energy

Figure 9 displays background-subtracted pulse profiles in five energy ranges from 0.1 keV to > 21 keV derived from the *ROSAT*, *ASCA*, and *RXTE* PCA data.

Striking features of the profiles are the simplicity and smoothness of the profiles, and the steady increase with energy in the relative amplitude of the narrower component of the double pulse. In marked contrast, the profiles of various other X-ray pulsars such as Vela X-1 and LMC X-4 are complex and vary widely over the same energy range. Such complexity may be caused by a multi-pole structure of the magnetic field that guides the accretion flow to the surface of the neutron star, giving rise to a multiplicity of hot spots and complicated patterns of emission from multiple accretion columns. In SMC X-1 it appears that the guiding field may be represented to a good approximation by a simple dipole inclined with respect to the spin axis. The different energy dependence of the two components, and the fact that the amplitude of the narrower one changes from less to more than that of the broader one precludes the possibility that they are caused by identical pencil beams emanating in opposite directions from the magnetic poles. Instead, the narrower pulse may be attributed to the pencil beam emanating from the accretion column above one pole, and the broader pulse to the fan beams emanating from the accretion columns above the two poles.

A second prominent feature is the variability with time and energy of the narrower pulse. In the energy bands where data from *ASCA* in April 1993 and from *RXTE* in January 1996 can be compared, there is a substantial change in the relative amplitudes of the two pulses which appears to be due to a change in the flux in the narrower pulse. Similar variability of the narrower pulse was reported by LRD in *Ginga* data from 1987, 1988, and 1989. In each of the three data sets displayed in Figure 9 the amplitude of the narrower pulse increases with energy, starting near zero in the *ROSAT* data below 1 keV, and rising above that of the wider pulse in the *RXTE* data above 21 keV.

X-ray production and radiative transfer in magnetized plasma has been computed by Nagel (1981) for slab and cylindrical geometries. In one particular case of cylindrical geometry with the magnetic field parallel to the axis, which serves as a model of an accretion column, the resulting radiation pattern has the form of combined pencil and fan beams, i.e., the escaping ordinary photons form a pencil beam with a maximum near 0° with respect to the axis, and the extraordinary photons form a fan beam with a

maximum at 90°. It may be plausible, therefore to model the SMC X-1 pattern as such a combination. If the broad pulse is identified with a fan beam, then its flat top can be attributed to the prolonged dwell near the minimum angle between the line of sight and the plane perpendicular to the dipole axis. If the narrow pulse is attributed to the pencil beam, its energy dependence and variability may be due to the energy dependence and variability of the opacity of the magnetized plasma through which the pencil beam propagates.

In Figure 10 we display the observed pulse profile of background-subtracted data from 2 to 21 keV (histogram) together with a model profile (crosses) computed for a radiation pattern consisting of an isotropic component plus combined pencil and fan beams. The pencil beam flux is represented by a Gaussian function of the angle, ρ, between the line of sight and the dipole axis, the fan beam flux by a Gaussian function of $90° - \rho$. We call Θ the inclination of the spin axis to the line of sight, and Ψ the angle between the spin axis and magnetic dipole axis. Then

$$\rho = \cos^{-1}[\sin\Theta\cos(\phi - \phi_0)\sin\Psi + \cos\Theta\cos\Psi]. \tag{4}$$

where ϕ is the pulse phase. The predicted flux was computed by the equation

$$F(\phi) = F_{\rm p}\exp\left(-\frac{\rho^2}{2w_{\rm p}^2}\right) + F_{\rm f}\exp\left(-\frac{(90° - \rho)^2}{2w_{\rm f}^2}\right) + F_0. \tag{5}$$

We set Θ to 60°, which implies equality between the the inclination of the spin axis and estimates of the orbit inclination, and Ψ to 27°. This combination of angles achieves the condition of a dwell of the fan beam near the line of sight. The other parameters were adjusted by eye and are listed in Table 6. We note that the pencil beam in this model is similar in angular width to that in the theoretical model of Nagel (1981) mentioned above. On the other hand, the fitted fan beam is substantially narrower than the computed one.

5. RANDOM INTENSITY FLUCTUATIONS

Power spectra of the random fluctuations in the *RXTE* PCA data in two energy ranges are displayed in the right-hand panels of Figure 11. The spectra were computed as follows: the data were divided into 53 segments of 256 seconds duration, the power spectrum of each segment was computed with the normalization of Leahy et al. (1983), the Poisson noise component of 2 was subtracted, and the result was divided by the mean count rate of the segment to obtain fractional RMS normalized powers. The 53 spectra were then averaged, and the powers due to five harmonics of the pulsed power, computed according to the method of Angelini et al. (1991), were subtracted. Finally, the resulting power spectra were logarithmically rebinned for display. The broken power laws and harmonic components that were fitted to the normalized spectra are displayed in the left-hand panels of Figure 11. The errors of the normalized powers before rebinning were all set equal to the expected RMS Poisson fluctuations computed as the quantity

$$\frac{2}{M}\left[\sum_{i=1}^{M}\left(1/c_i^2\right)\right]^{1/2}, \tag{6}$$

where c_i is the count rate during the ith data segment, and M is the number of segments.

A marked difference is apparent between the forms of the power spectrum in the low and high energy channels. The spectrum in the 2.0-3.4 keV range is fitted by a single power law with an index of 0.51;

the 3.4-21 keV spectrum conforms to a broken power law with indices of 0.45 and 1.76 with a sharp break at 3.3 Hz. Both spectra show a positive deviation from the power-law fit around 0.06 Hz which may be attributed to quasi-periodic oscillation (QPO).

The break we find in the power spectrum above 3.4 keV is similar to those found by Takeshima (1994) in *Ginga* observations of several pulsars. He fitted the power spectra with broken power laws, and found breaks occurring near the fundamental pulsar frequencies. In his analysis of data from the second and third *Ginga* observations of SMC X-1 listed in Table 4, he found breaks at 2.93 Hz and 1.79 Hz.

The difference between the power spectra that we find in the high and low-energy portions of the X-ray flux may be a clue to the effect of magnetic field intensity on the frequency spectrum of emission fluctuations. The flux in the low-energy channel may be dominated by radiation emitted from the accretion disk where the magnetic field is relatively weak. Most of the flux in the high-energy channels certainly arises from the accretion column and hot spot near the surface of the neutron star, where the magnetic field is strong. The strong field may suppress the fluctuations responsible for low-frequency red noise, thereby causing the abrupt decrease in the logarithmic slope of the power spectrum below 3.3 Hz.

6. Summary

The principal results in this paper are as follows:

The ASM light curve of SMC X-1 confirms the presence of a high-low state cyclic variation of the X-ray flux, and shows that the cycle duration varied from ~ 50 to ~ 60 days. The BATSE data show that the cyclic variation is a persistent phenomenon.

Results from pointed observations show that the uneclipsed flux of SMC X-1 in the high state is more than an order of magnitude greater than in the low state. In contrast, the eclipsed flux, consists of X-rays scattered from circumsource matter, differs by no more than a factor of ~ 2 between the two states, and the spectrum shape does not change significantly. Thus, the high-low cyclic variation is not caused by either a change in the luminosity of the source, or a redistribution of the energy. Rather, it must be the result of a quasi-periodic blockage of the line of sight.

In a simple model of occultation by a ring of non-interacting particles at the rim of a tilted accretion disk, the forced precession caused solely by the gravity of the companion star would have a period of about half the observed long-term cycle duration. Similar differences are found between the predicted precession periods for the simple model and the observed long-term cycle periods of Her X-1 and LMC X-4. It has been shown that more detailed and realistic models of precessing accretion disks that take account of the effects of the accretion rate, accretion energy conversion efficiency, and viscosity in the disk, can be adjusted to cause model disks to tilt and precess with periods in agreement with the observed long-term cycles. We therefore conclude that the high-low state cycle in the X-ray flux from SMC X-1, like the similar cycles of Her X-1 and LMC X-4, is the result of quasi-periodic occultation by a precessing tilted accretion disk.

Timing analysis of the 0.71 second pulses shows a continuation of the decay of the binary orbit through 1996 January at a rate consistent with previous results.

The pulse period has continued its apparently monotonic decrease at a gradually decreasing rate.

The pulse profile can be modeled with fair accuracy by a three component radiation pattern consisting of an isotropic component plus combined pencil and fan beams symmetric about an axis inclined at 27° from the spin axis, with the spin axis inclined at 60° to the line of sight.

The power spectrum of the flux recorded by *RXTE* in energy channels below 3.4 keV is fitted by a single power law with index 0.51 over the frequency range from 0.01 to 32 Hz. In marked contrast, the power spectrum in energy channels above 3.4 keV is fitted by a broken power law with a sharp decrease in index from 1.76 above 3.3 Hz to 0.45 below. The low-energy flux may be dominated by radiation emitted from the accretion disk where the magnetic field is relatively weak. The high-energy flux is emitted primarily in regions of strong magnetic field which may suppress the emission fluctuations that cause the low-frequency red noise.

In both the high and low-energy power spectra there is a positive deviation from the fitted power law around 0.06 Hz that may be QPO.

We used the *XSPEC* X-ray spectral fitting program for our spectral analysis. Archival *ROSAT* and *ASCA* data was obtained with the use of the High Energy Astrophysics Science Archive Research Center Online Service, provided by the NASA/Goddard Space Flight Center. We thank Jane Turner and Ken Ebisawa of the *user support teams for advice on reducing and analyzing ROSAT* and *ASCA* data, and Edward Morgan of MIT for assistance in the use of *RXTE* data acquired during the in-orbit calibration (IOC) period of operation. We specially thank the referee, J. van Paradijs, for his careful reading and valuable suggestions for improvements in the manuscript.

REFERENCES

Angelini, L., Stella, L., & White, N. E., 1991, ApJ 371, 332

Aschenbach, B., 1988, Appl. Opt. 27, 1404

Blondin, J. M., & Woo, J. W., 1995, ApJ 445, 889

Bonnet-Bidaud, J. M., & van der Klis, M., 1981, A&A 97, 134

Clark, G. W., Remillard, R. A., & Woo, J. W., 1997, ApJ 474, L111

Cooke, B. A. et al., 1978, MNRAS 182, 489

Darbro, W., Ghosh, P., Elsner, R. F., Weisskopf, M. C., Sutherland, P. G., & Grindlay, J. E., 1981, ApJ 246, 231

Davison, P. J. N., 1977, MNRAS 179, 15P

Deeter, J. E., Boynton, P. E., & Pravdo, S. H., 1981, ApJ 247, 1003

Eggelton, P. P., 1983, ApJ 268, 368

Fishman, G. J. et al., 1994, ApJS 92, 229

Gerend, D., & Boynton, P. E., 1976, ApJ 209, 562

Gruber, D. E., & Rothschild, R. E., 1984, ApJ 283, 546

Hammerschlag-Hensberge, G., Kallman, T. R., & Howarth, I. D., 1984, ApJ 283, 249

Harmon, B. A., et al., 1992, in AIP Conf. Proc. 280, Compton Gamma-Ray Observatory, ed. M. Friedlander,N. Gehrels, & D. J. Macomb, p. 314, St. Louis, MO

Hayashida, K., Inoue, H., Koyama, K., Awaki, H., & Takano, S., 1989, PASJ 41, 373

Heemskerk, M. H. M., & van Paradijs, J., 1989, A&A 223, 154

Henry, P., & Schrier, E., 1977, ApJ 212, L13

Howarth, I. D., 1982, MNRAS 198, 289

Hutchings, J. B., Crampton, D., Cowley, A. P., & Osmer, P. S., 1977, ApJ 217, 186

Ilovaisky, S. A., Chevalier, C., Motch, C., Pakull, M., van Paradijs, J., & Lub, J., 1984, A&A 140, 251

Iping, R. C., & Petterson, J. A., 1990, A&A 239,221

Jahoda, K., Swank, J. H., Giles, A. B., Stark, M. J., Strohmayer, T., Zhang, W., & Morgan, E., 1996, in EUV, X-ray and Gamma-ray Instrumentation for X-ray Astronomy VII, ed. O. H. W. Siegmund and M. A. Grummin, SPIE, 2808, 59

Kahabka, P., & Pietsch, W., 1996, A&A 312, 919

Katz, J. I., 1973, Nature Phys. Sci. 246, 87

Khruzina, T. S., & Cherepashchuk, A. M., 1987, AZh 64, 345

Leahy, D. A., Darbro, W., Elsner, R. F., Weisskopf, M. C., Kahn, S., Sutherland, P. G., & Grindlay, J. E., 1983, ApJ 266, 160

Leong, C., Kellogg, E., Gursky, H., Tannenbaum, H., & Giacconi, R., 1971, ApJ, 170, L67

Levine, A., Rappaport, S., Deeter, J. E., Boynton, P. E., & Nagase, F., 1993, (LRD) ApJ 410, 328

Levine, A. M., Bradt, H., Cui, W., Jernigan, J. G., Morgan, E. H., Remillard, R., Shirey, R. E., & Smith, D. A., 1996, ApJ 469, L33

Levine, A. M., & Jernigan, J. G., 1982, ApJ 262, 294

Liller, W., 1973, ApJ 184, L37

Lucke, R., Yentis, D., Friedman, H., Fritz, G., & Shulman, S., 1976, ApJ 206, L25

Makino, F., & the ASTRO-C team, 1987, Ap. Lett. Comm. 25, 223

Morrison, R., & McCammon, D., 1983, ApJ 270, 119

Nagel, W., 1981, ApJ 251, 278

Pfeffermann, E. et al., 1987, SPIE 733, 519

Price, R. E., Groves, D. J., Rodrigues, R. M., Seward, F. D., Swift, C. D., & Toor, A., 1971, ApJ 168, L7

Priedhorsky, W. C., & Holt, S. S., 1987, Space Science Reviews 45, 291

Primini, F., Rappaport, S., & Joss, P. C., 1977, ApJ 217, 543

Pringle, J. E., 1996, MNRAS, 281, 357

Schreier, E., Giacconi, R., Gursky, H., Kellogg, E., & Tananbaum, H., 1972, ApJ 178, L71

Reynolds, A. P., Hilditch, R. W., Bell, S. A., & Hill, G., 1993, A&A 261, 337

Takeshima, T., 1994, PhD thesis, University of Tokyo

Tanaka, Y., Inoue, H., & Holt, S. S., 1994, PASJ 46, L37

Tjemkes, S. A., Zuiderwijk, E. J., & van Paradijs, J., 1986, A&A 154, 77

Trümper, J., 1983, Adv. Space Res. 2, 241

Tuohy, I. R., & Rapley, C. G., 1975, ApJ 198, L69

Turner, M. J. L. et al., 1989, PASJ 41, 345

van Paradijs, J., & Zuiderwijk, E., 1977, A&A 61, L19

Webster, B. L., Martin, W. L., Feast, M. W., & Andrews, P. J., 1972, Nature, Phys. Sci. 240, 183

Whitlock, L., & Lochner, J. C., 1994, ApJ 437, 841

Woo, J. W., Clark, G. W., Blondin, J. M., Kallman, T. R., & Nagase, F., 1995, ApJ 445, 896

Woo, J. W., Clark, G. W., & Levine, A. M., 1995, ApJ 449, 880

Yentis, D., Shulman, S., McKee, J. D., & Rose, W. K., 1977, Astrophys. Lett. 19, 53

Zhang, S. N., Robinson, C. R., Wilson, R. B., Harmon, B. A., Scott, D. M., & Remillard, R., 1996, IAU Circ. 6468

This plano tables was prepared with the AAS LaTeX macros v4.0.

TABLE 1
SUMMARY OF POINTED OBSERVATIONS

Instrument and ID	Start Time-Stop Time	Phases[a]	Exposure (s)	State	ref
Ginga	1989 Jul 30.78-Aug 3.20[b]	0.34 – 0.21	74240	high	1
ROSAT 1	1991 Oct 7.17-8.13	0.48 – -0.29	16634	high	2
ROSAT C	1991 Oct 16.31-19.98	-0.18 – -0.24	22173	low	3
ROSAT 2	1992 Sep 30.71-Oct 2.59	-0.15 – 0.33	8932	low	2
ROSAT 3	1993 Jun 2.99-4.20	-0.13 – 0.18	11864	high	2
ASCA 1	1993 Apr 26.94-27.97	0.35 – -0.39	34507	high	
ASCA 2	1995 Oct 18.79-19.88	-0.17 – 0.11	30628	low	
RXTE	1996 Jan 11.00-11.23	0.47 – -0.47	14536	high	

[a]Binary orbit phase range on the (-0.5,0.5) interval. All observations span less than one binary orbit.

[b]SMC X-1 was observed for more than one binary orbit. Only a subset of the data actually collected is described here.

REFERENCES.— (1) Woo, et al. 1995; (2) Clark, et al. 1997; (3) Kahabka & Pietsch 1996.

TABLE 2
AVERAGE COUNT RATES IN SEVEN ENERGY RANGES OF *RXTE* DATA

	Average Count Rates (counts s^{-1})	
Energy Range (keV)	SMC X-1 +Background	Earth Occulted
2.0-3.4	43.5	5.7
3.4-5.8	173	5.0
5.8-8.6	173	4.6
8.6-21	238	21
21-60	74	53

TABLE 3
FITTED VALUES OF THE SPECTRAL FUNCTION PARAMETERS

Parameter	Value	(1σ error)
$N_{\rm H}(10^{20}$ cm$^{-2})$	5.9	(4.2)
$E_{\rm bb}$ (keV)	0.25	(0.02)
$I_{\rm bb}$ (10^{-3} photons cm^{-2} s^{-1} keV^{-1})	9.	(3)
α	-0.2	(0.1)
$I_{\rm pl}(10^{-5}$ photons cm^{-2} s^{-1} keV^{-1})	9.8	(3.1)
$E_{\rm c}$ (keV)	6.5	(0.4)
$E_{\rm f}$ (keV)	5.9	(0.4)
χ^2_ν	3.96	

TABLE 4
Summary of Mid-Eclipse Times and Pulse Period Measurements

Observatory	$T^a_{\pi/2}(1\sigma)$ (MJED)	N	$P_{\rm pulse}(1\sigma)$ s	Reference
Uhuru	40963.99(2)	−481	.....	Schreier et al. 1972
Uhuru	41114.2[b]	.....	0.71748(26)	Henry & Schreier 1977
Aerobee	41999.6[b]	.....	0.7164(2)	Yentis et al. 1977
Copernicus	42275.65(4)	−144	.....	Tuohy & Rapley 1975
Apollo-Soyuz	42613.8[b]	.....	0.7151(2)	Yentis et al. 1977
SAS 3	42836.1828(2)	0	0.71488585(4)	Primini et al. 1977
Ariel V	42999.6567(16)	42	0.7147337(12)	Davison 1977
Einstein	43985.907[b]	.....	0.713684(32)	Darbro et al. 1981
COS B	43116.4448(22)	72	.....	Bonnet-Bidaud et al. 1981
Ginga	46942.47237(15)	1055	0.710592116(36)	LRD
Ginga	47401.744476(7)	1173	0.7101406720(15)	LRD
Ginga	47740.35906(3)	1260	0.709809901(32)	LRD
ROSAT 1	48534.34786(35)	1464	0.70911393(34)	Present work
ROSAT 2	48892.4191[b]	1556	0.7088166(6)	Present work
ASCA	49102.59109(82)	1610	0.7086390(9)	Present work
ROSAT 3	49137.61911(50)	1619	0.7085992(5)	Present work
RXTE	50091.170(63)	1864	0.70767331(8)	Present work

[a]Mid-eclipse time, equivalent to time when mean longitude l equals $\pi/2$ for a circular orbit (c.f. Deeter, Boynton, & Pravdo 1981).

[b]Set to predicted mid-eclipse times

TABLE 5
PARAMETERS OF THE SPIN-UP AND ORBITAL DECAY

	Value (1σ uncertainty)	
Parameter	Present Work	LRD
$a_{\rm x} \sin i$ (lt-s)	.....	53.4876
Eccentricity	.....	< 0.00004
$\dot{P}_{\rm pulse}/P_{\rm pulse}$ (yr^{-1})	$-4.52(2) \times 10^{-4}$ [a]	$-5.30(2) \times 10^{-4}$
a_0 [b] (MJED)	42836.18278(20)	42836.18277(20)
a_1 [b] (days)	3.89229090(43)	3.89229118(48)
a_2 [b] (days)	$-6.953(28) \times 10^{-8}$	$-6.97(3) \times 10^{-8}$
$\dot{P}_{\rm orb}/P_{\rm orb}$ (yr^{-1})	$-3.353(14) \times 10^{-6}$ [a]	$-3.36(3) \times 10^{-6}$

[a]Evaluated at MJED 50000.
[b]Center time of the $N^{\rm th}$ eclipse is given by $t_{\rm N} = a_0 + a_1 N + a_2 N^2$.

TABLE 6
COEFFICIENTS OF THE QUADRATIC FIT TO THE PULSE PERIOD DATA

Parameter	Value	
p_0	0.707753	s
p_1	-8.75×10^{-6}	s day^{-1}
p_2	1.68×10^{-11}	s day^{-2}
t_0	2450000.5	JD

$$P_{\rm pulse} = p_0 + p_1(t - t_0) + p_2(t - t_0)^2.$$

Fig. 1.— *CGRO* BATSE and *RXTE* ASM (1.5-12 keV)light curves of SMC X-1. The time of the start of each of the pointed observations is indicated on this figure by R for *ROSAT*, A for *ASCA*, and X for *RXTE*.

Fig. 2.— Time intervals between successive high/low transitions of SMC X-1. The transition times are obtained from crossings of 2 counts s^{-1} in the ASM light curve.

Fig. 3.— Deviations from the average count rates, given in terms of a reduced chi-squared statistic, of four sections of the BATSE light curve, of the entire BATSE light curve, and the ASM light curve when folded at various trial periods. The horizontal bars indicate the expected width (FWHM) of a peak corresponding to a sinusoidal variation with constant period.

Fig. 4.— Count rates of SMC X-1 as a function of orbital phase for the pointed observations. The *ROSAT* PSPC region C count rates are corrected for off-axis vignetting. Dashed lines at orbital phase ± 0.07 indicate the end of immersion and beginning of emersion of the eclipse transitions observed in the high state.

Fig. 5.— Observed photon number spectra during eclipses (orbital phase in the range -0.07 to +0.07) and the computed spectra (solid lines) for a single fitted model.

Fig. 6.— Pulse arrival-time delays plotted against orbital phase together with the fitted curves of predicted delays and residuals.

Fig. 7.— Differences between the measured values of eclipse center times ($T_{\pi/2}$) and values computed for a constant orbital period ($P_{\rm orb}$=3.892188). The solid curve is the fitted function (see Table 5) which includes a linear decrease of the orbital period.

Fig. 8.— Inferred intrinsic pulse period plotted against time together with a fitted quadratic and residuals.

Fig. 9.— Pulse profiles in various energy bands derived from the *ROSAT* 1, *ASCA* 1, and *RXTE* data.

Fig. 10.— Computed pulse profile (crosses) modeled by pencil and fan beams and fitted to the observed average 2-21 keV pulse profile (histogram) derived from the *RXTE* PCA data.

Fig. 11.— Left panels: Fitted harmonic and continuum components of the power spectra in two energy bands of *RXTE* PCA data with times corrected for orbital motion. Right panels: Power spectra after subtraction of the harmonic components.

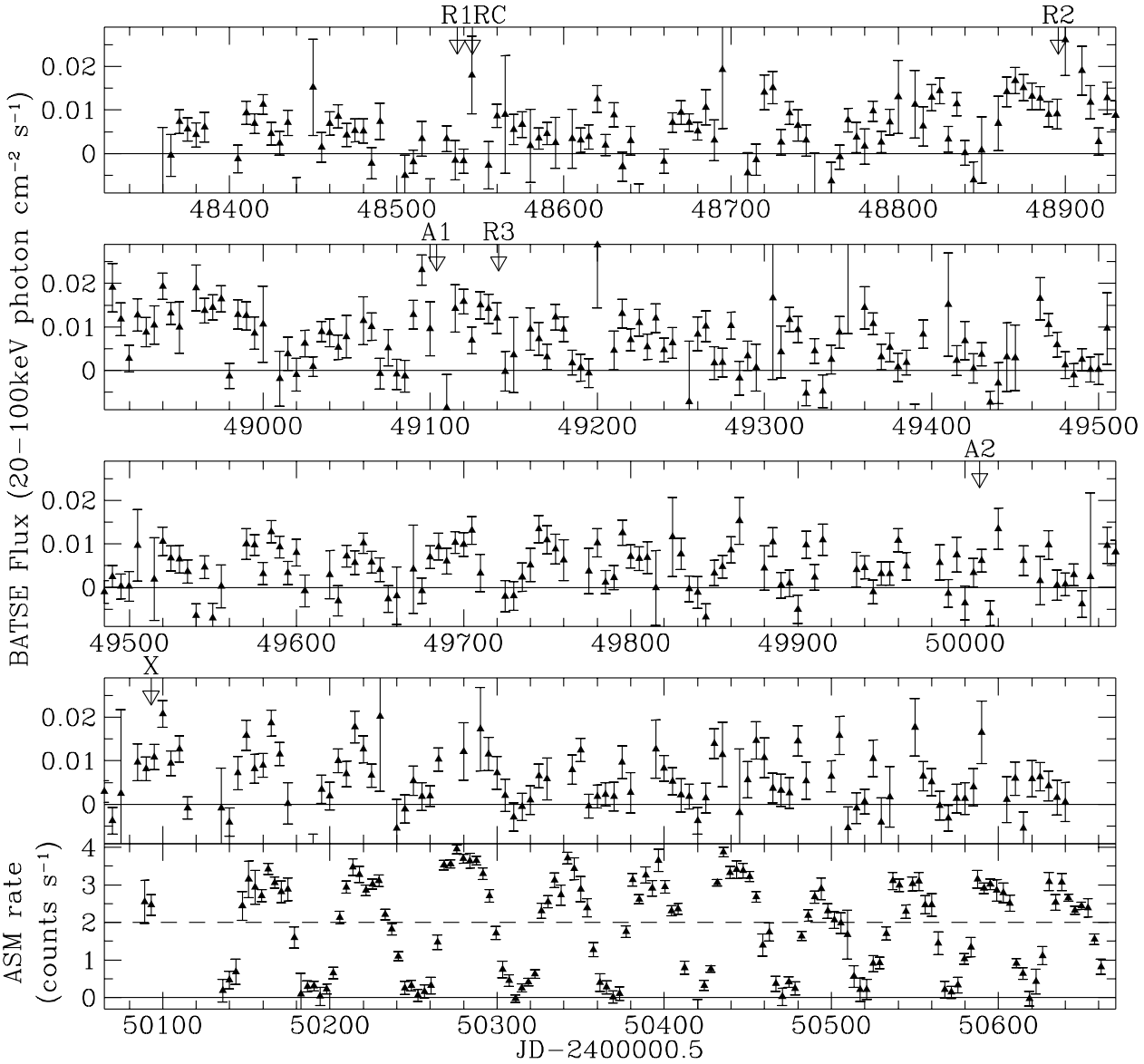
R1RC
R2
A1
R3
A2
X
BATSE Flux (20−100keV photon cm⁻² s⁻¹)
ASM rate (counts s⁻¹)
JD−2400000.5

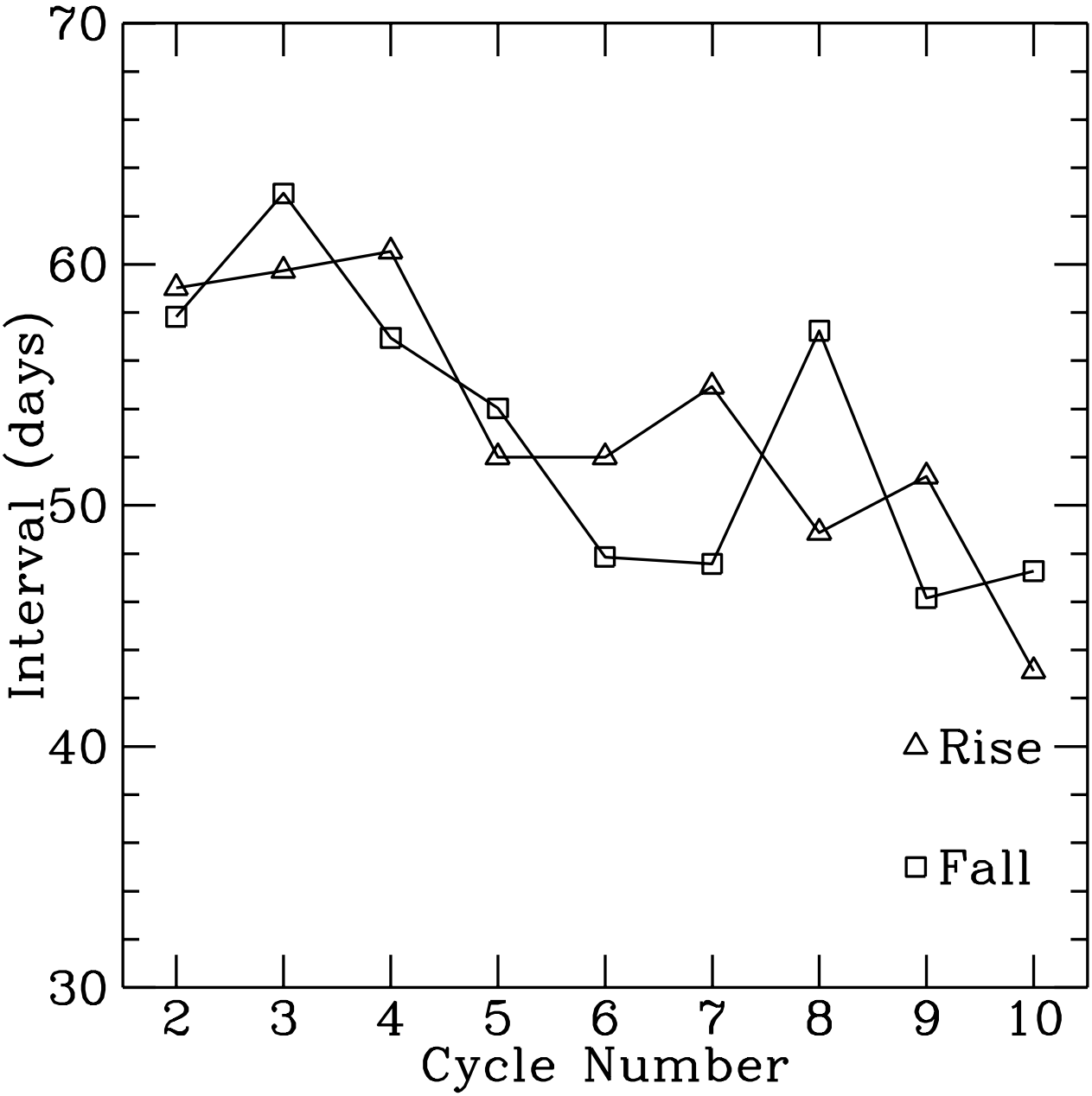
70
60
50
40
30
Interval (days)
2
3
4
5
6
7
8
9
10
Cycle Number
Rise
Fall

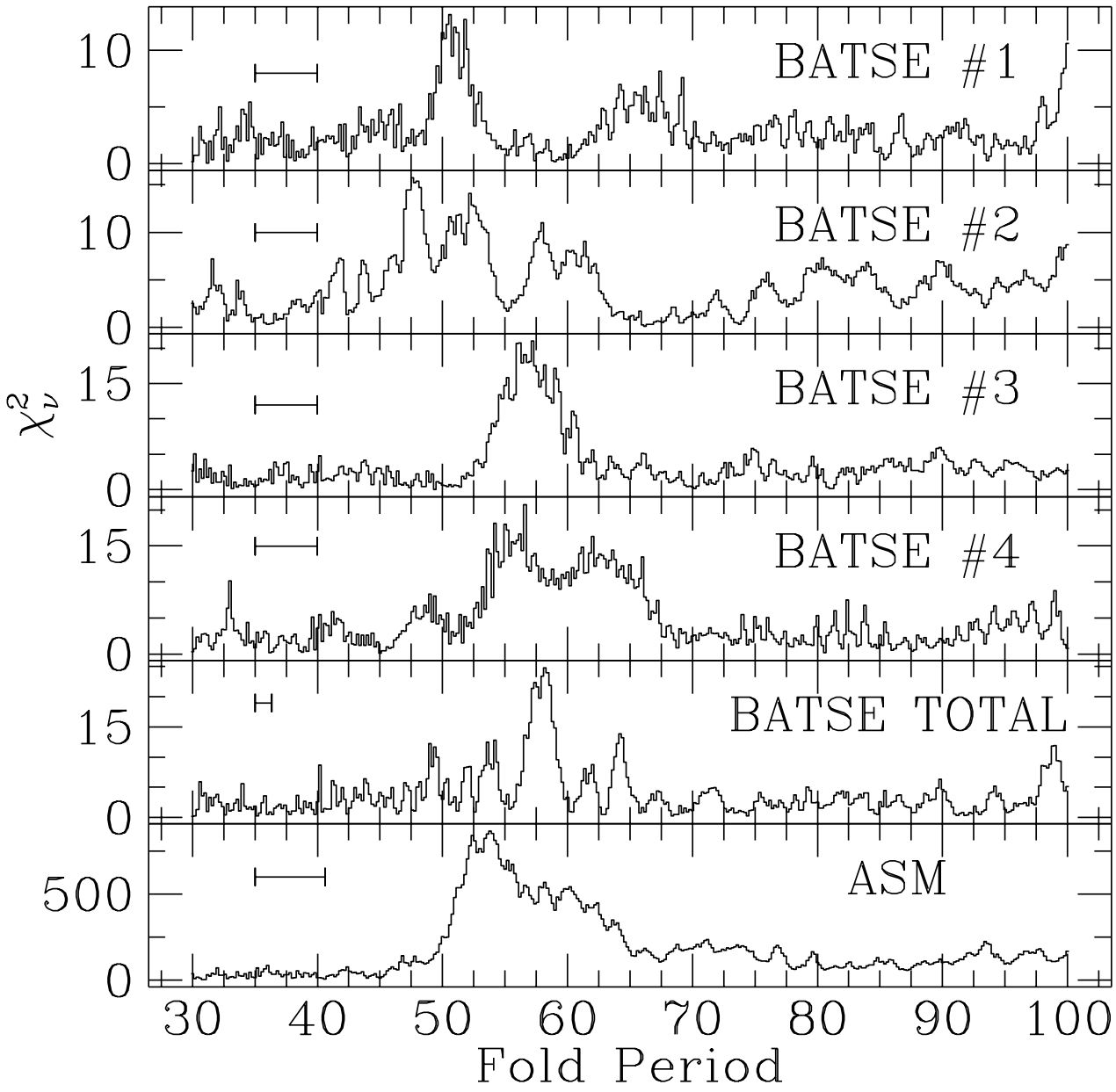
BATSE #1
BATSE #2
BATSE #3
BATSE #4
BATSE TOTAL
ASM
χ^2_ν
10
0
10
0
15
0
15
0
15
0
500
0
30
40
50
60
70
80
90
100
Fold Period

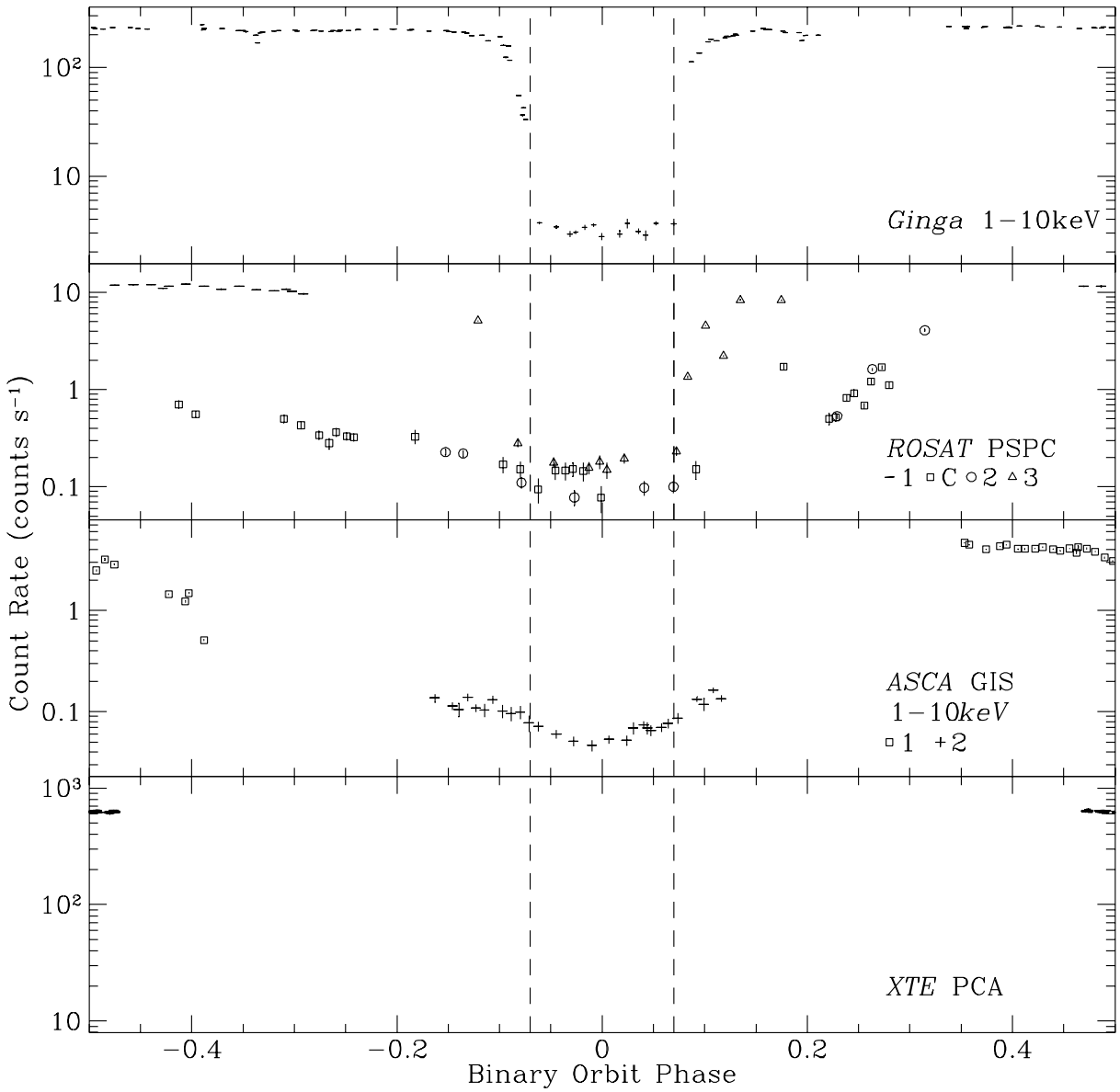
Ginga 1−10keV
ROSAT PSPC
−1 □ C ○ 2 △ 3
ASCA GIS
1−10keV
□ 1 + 2
XTE PCA
Count Rate (counts s⁻¹)
Binary Orbit Phase
10²
10
1
0.1
10³
−0.4
−0.2
0
0.2
0.4

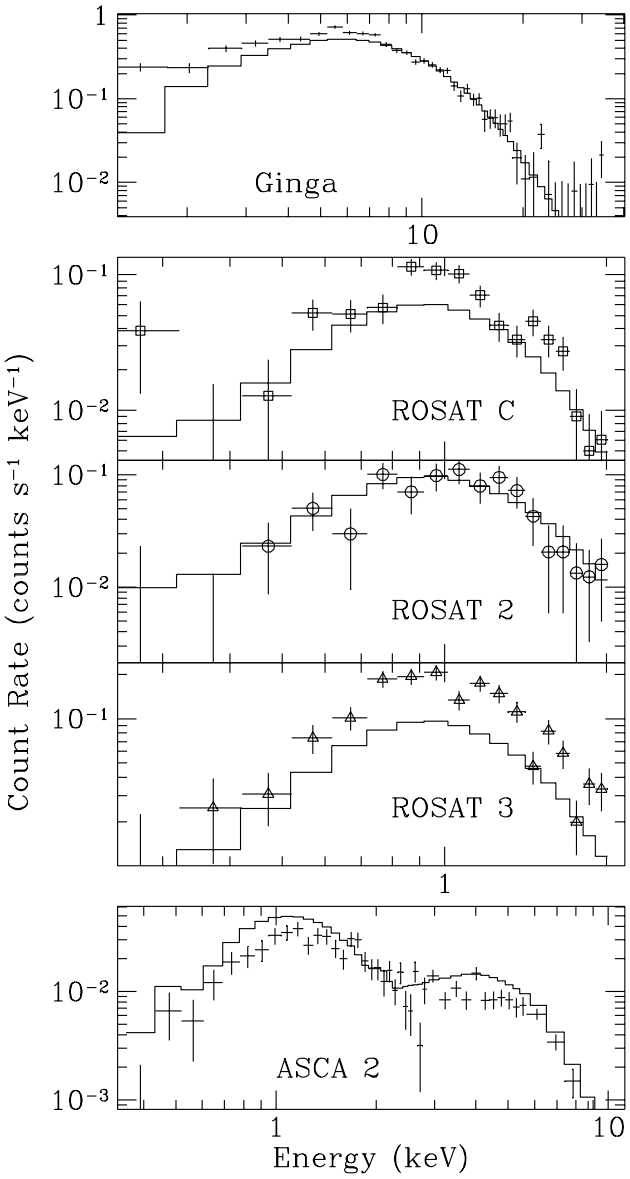
Ginga
ROSAT C
ROSAT 2
ROSAT 3
ASCA 2
Count Rate (counts s^{-1} keV^{-1})
Energy (keV)

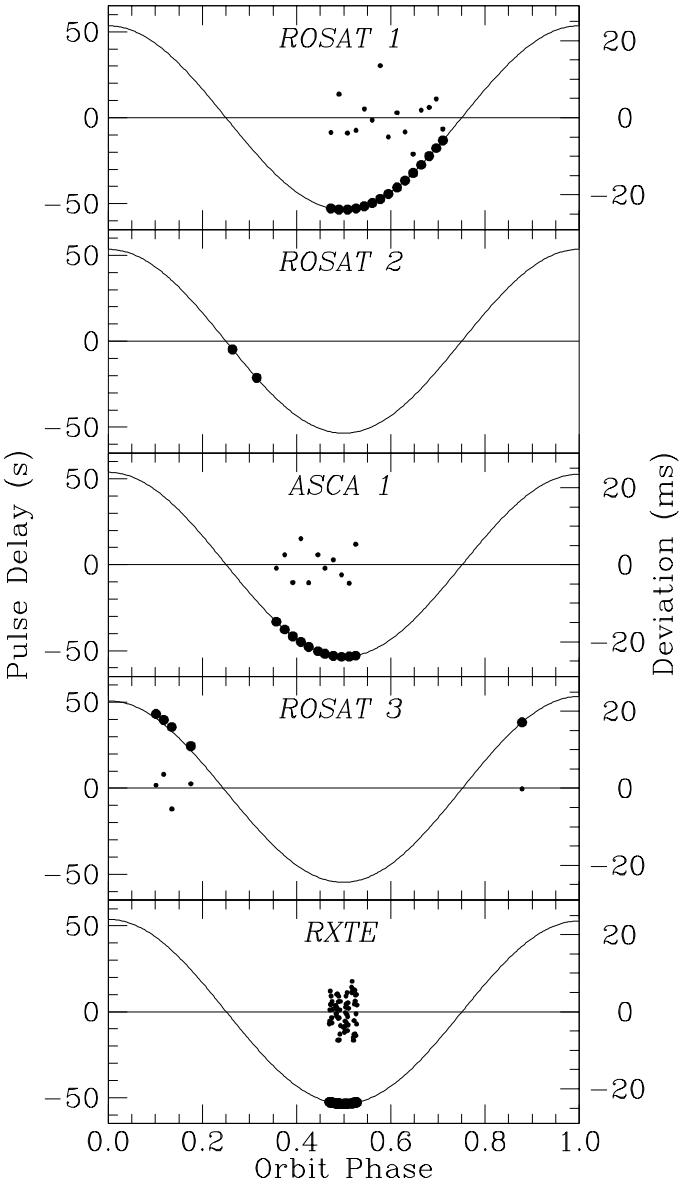
ROSAT 1
ROSAT 2
ASCA 1
ROSAT 3
RXTE
Pulse Delay (s)
Deviation (ms)
Orbit Phase
50
0
−50
20
0
−20
0.0
0.2
0.4
0.6
0.8
1.0

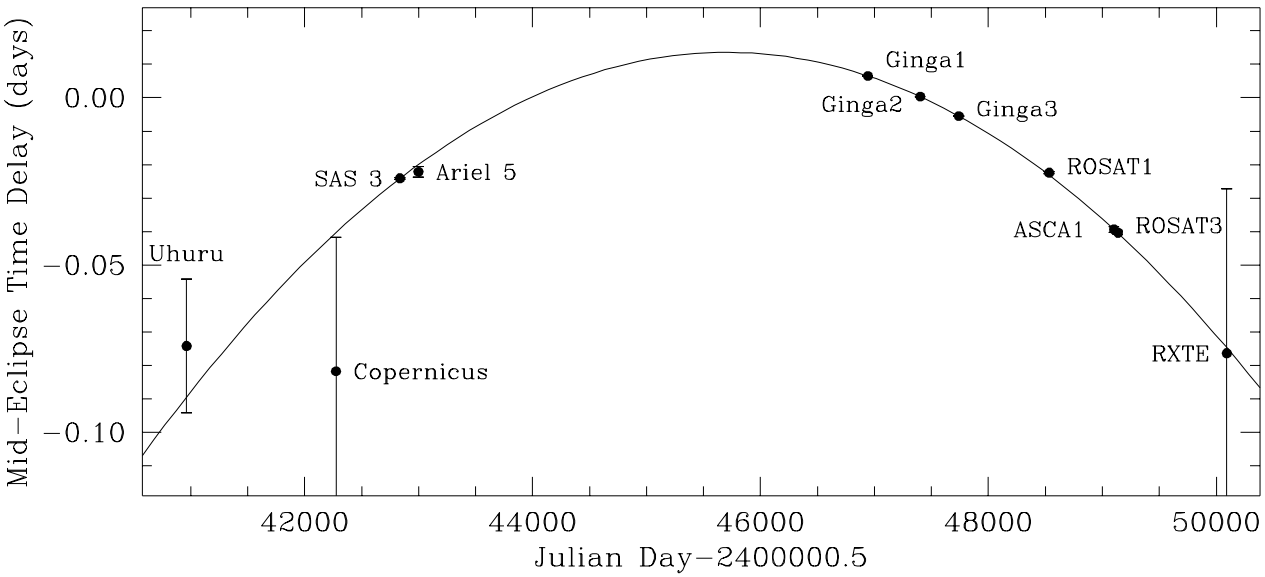
Mid−Eclipse Time Delay (days)
0.00
−0.05
−0.10
42000
44000
46000
48000
50000
Julian Day−2400000.5
Uhuru
SAS 3
Ariel 5
Copernicus
Ginga1
Ginga2
Ginga3
ROSAT1
ASCA1
ROSAT3
RXTE

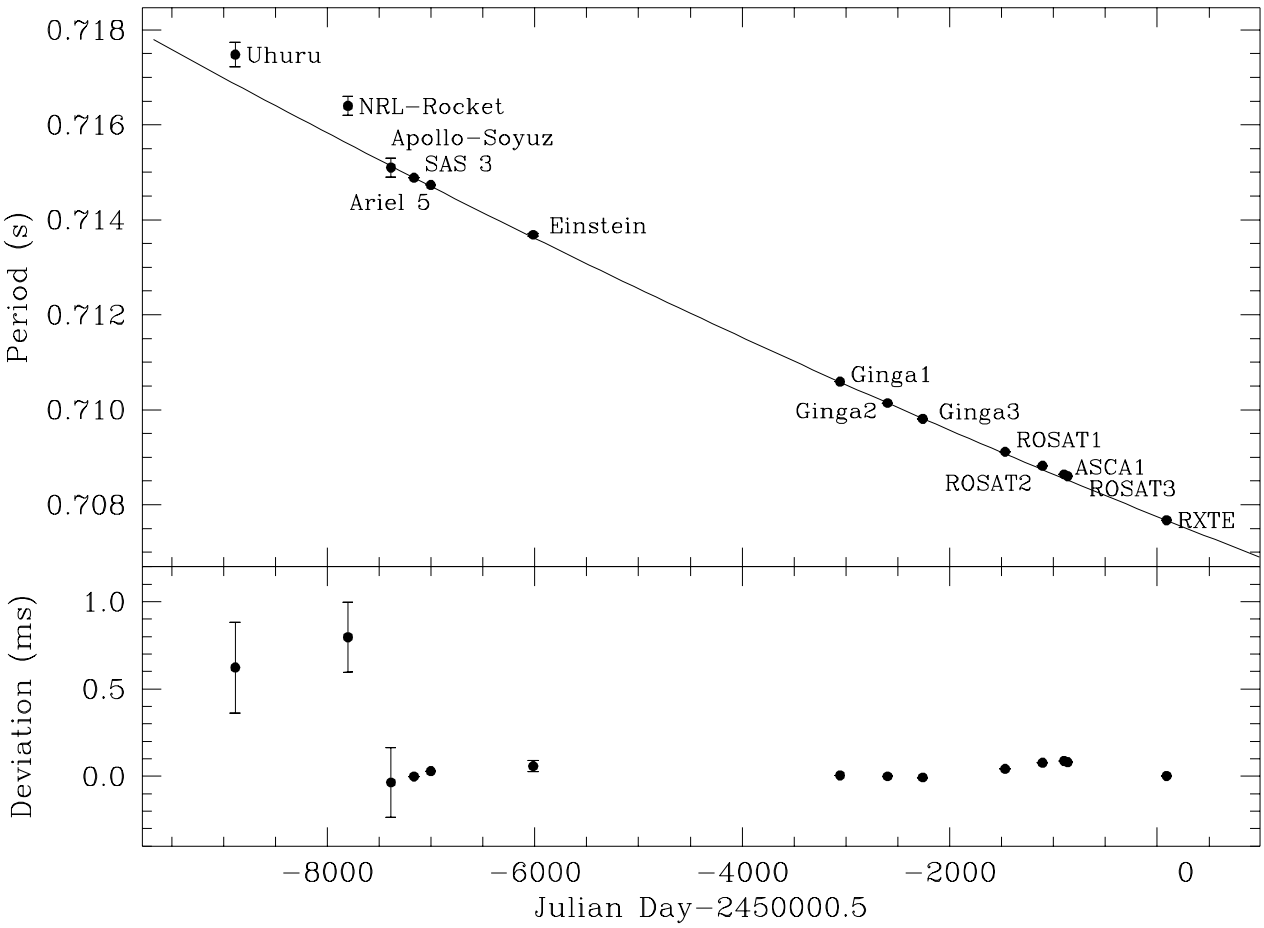
0.718
0.716
0.714
0.712
0.710
0.708
Period (s)
Uhuru
NRL−Rocket
Apollo−Soyuz
SAS 3
Ariel 5
Einstein
Ginga1
Ginga2
Ginga3
ROSAT1
ASCA1
ROSAT2
ROSAT3
RXTE
1.0
0.5
0.0
Deviation (ms)
−8000
−6000
−4000
−2000
0
Julian Day−2450000.5

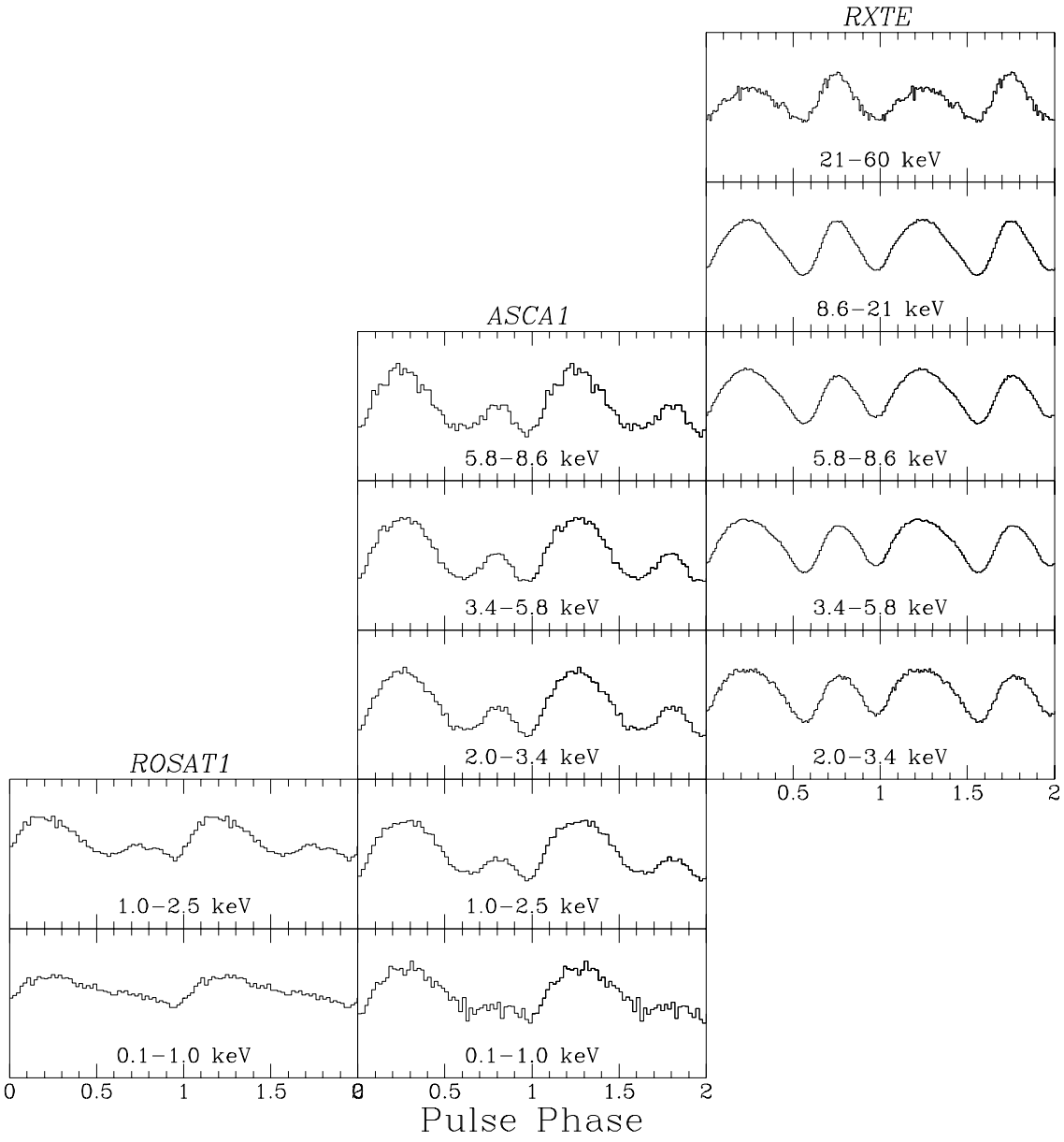
RXTE
21−60 keV
8.6−21 keV
ASCA1
5.8−8.6 keV
5.8−8.6 keV
3.4−5.8 keV
3.4−5.8 keV
2.0−3.4 keV
2.0−3.4 keV
ROSAT1
1.0−2.5 keV
1.0−2.5 keV
0.1−1.0 keV
0.1−1.0 keV
0
0.5
1
1.5
2
Pulse Phase

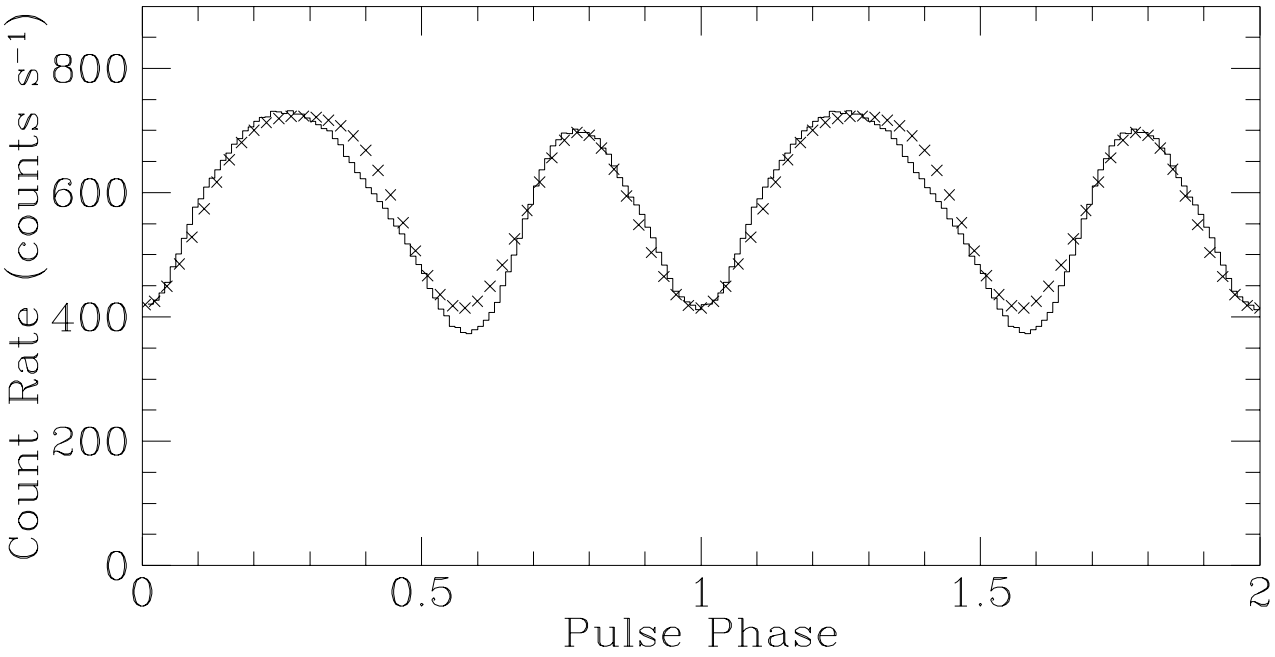
Count Rate (counts s^{-1})
0
200
400
600
800
0
0.5
1
1.5
2
Pulse Phase

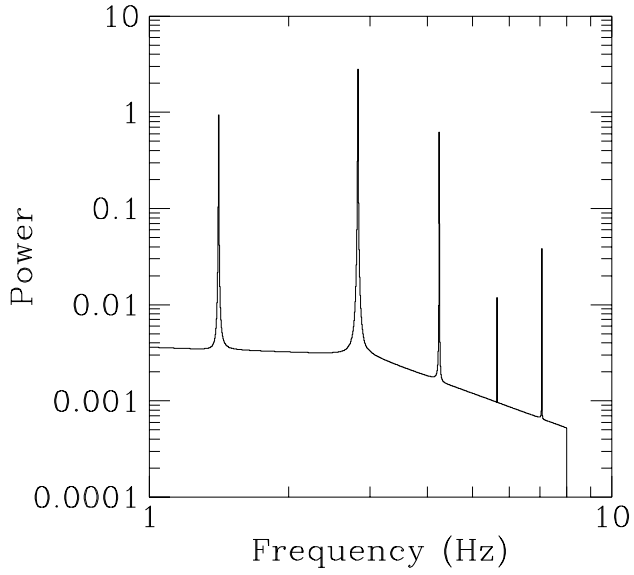
Power
Frequency (Hz)

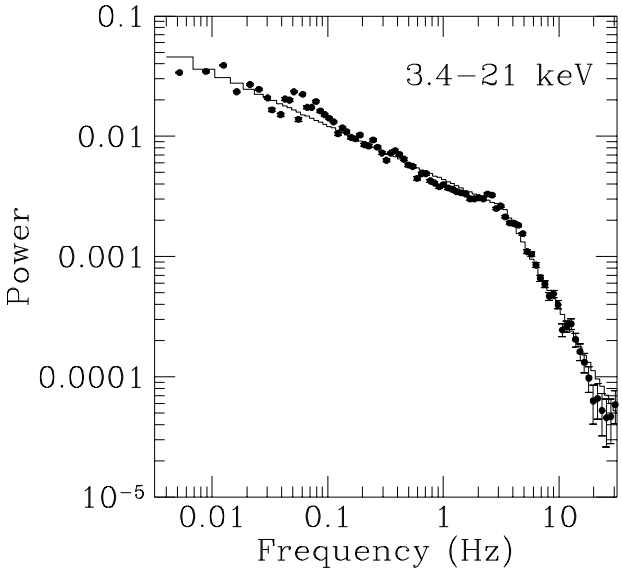
3.4−21 keV
Power
Frequency (Hz)

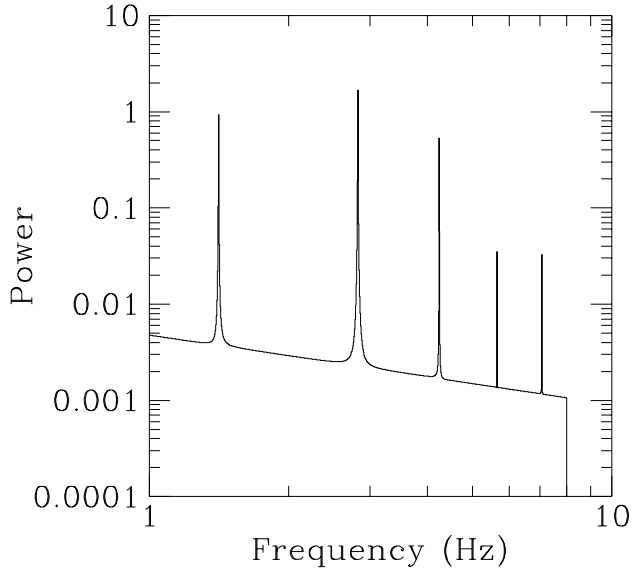
Power
Frequency (Hz)

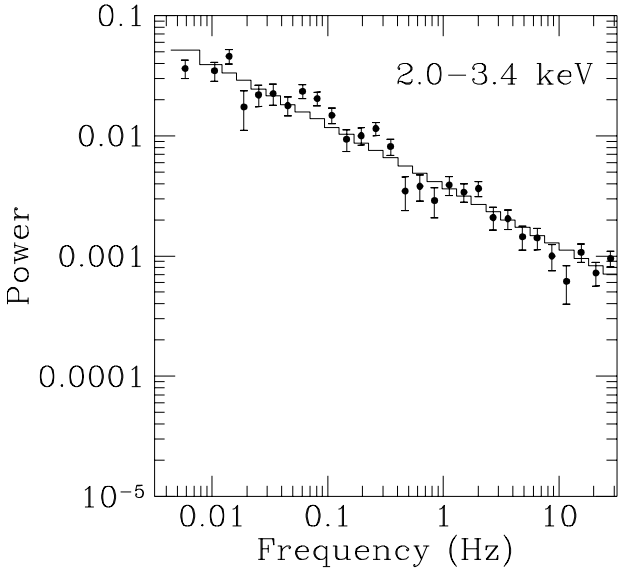
2.0−3.4 keV
Power
Frequency (Hz)